Coaxial Nickel-Poly(Vinylidene Fluoride Trifluoroethylene) Nanowires for Magnetoelectric Applications

Chess Boughey, Yonatan Calahorra, Anuja Datta[#] and Sohini Kar-Narayan*

Department of Materials Science, University of Cambridge, 27 Charles Babbage Road, Cambridge CB3 0FS, UK.

[#]Present Affiliation: School of Applied & Interdisciplinary Sciences, Indian Association for the Cultivation of Science, 2A/2B Raja S.C. Mullick Road, Jadavpur, Kolkata-700 032, India.

**sk568@cam.ac.uk*

Abstract

Magnetoelectric (ME) composite materials, in which the coupling between magnetostricitve and piezoelectric effects is achieved, are potential candidates for multifunctional devices where the interplay between electrical, magnetic and mechanical properties of these structures can be fully exploited. Nanostructured composites are particularly interesting due to the enhancement of ME coupling expected at the nanoscale. However, direct studies of ME coupling in nanocomposites by scanning probe techniques are rare due to the complex interplay of forces at play, including those arising from electrostatic, magnetic and electromechanical interactions. In this work, the ME coupling of coaxial nickel - polyvinylidene fluoride trifluoroethylene [Ni-P(VDF-TrFE)] composite nanowires, fabricated by a scalable template-wetting based technique, is studied using a systematic sequence of scanning probe techniques. Individual ME nanowires were subjected to an electric field sufficient for ferroelectric poling in piezo-response force microscopy (PFM) mode, while magnetic force microscopy (MFM) was used

to measure localised changes in magnetization as a result of electrical poling. Kelvin probe force microscopy (KPFM) measurements of surface potential were conducted to eliminate for the effect of contact potential differences during these measurements. An inverse, static, magnetoelectric coupling coefficient of ~1 x 10^{-11} s m^{-1} was found in our coaxial nanocomposite nanowires, comparable to other types of planar composites studied in this work, despite having an inferior piezoelectric-to-magnetostrictive volume ratio. The efficient ME coupling in our coaxial nanowires is attributed to the larger surface-to-volume interfacial contact between Ni and P(VDF-TrFE), and is promising for future integration into ME composite devices such as magnetic field sensors or energy harvesters.

Keywords

Magnetoelectric coupling, coaxial nanocomposite nanowires, magnetic force microscopy, Kelvin probe force microscopy, piezoelectric-magnetostrictive composites, magnetic field sensing.

Introduction

Stray magnetic fields and parasitic magnetic noise are found in many locations, from overhead power transmission cables, computers and electronic devices. The ubiquitous nature of this noise offers an advantage for use as a source of ambient energy over mechanical ambient vibrations for instance, which can be intermittent and produce variable power densities [1,2]. The need for cleaner and more sustainable energy sources for wireless low-power electronics is becoming increasingly in demand as the number of smart devices increases. In typical homes, the 50 / 60 Hz electromagnetic radiation which emanates from wiring can reach 0.01 Gauss - 10 Gauss [3] and in industrial locations with heavy electrical machinery, the magnetic field strength may even exceed 100 Gauss [3]. At the same time, there is a need for efficient and cost-effective sensors that are sensitive to small magnetic fields, for applications as diverse as

medical devices, communications and even power electronics [4]. Magnetoelectric (ME) devices provide an attractive route to achieving the above due to their ability to inter-convert magnetic and electric signals.

The ME effect refers to the induced electrical polarisation in a material under an applied magnetic field. The ME coupling coefficient, to a linear approximation, is defined by

$$\alpha_{\mathrm{ij}} = \frac{\partial P_{\mathrm{i}}}{\partial H_{\mathrm{j}}} \tag{1}$$

and sometimes

$$\alpha_{\mathrm{ij}}^{\mathrm{E}} = \frac{\Delta E_i}{\Delta H_j} \tag{2}$$

is used, while the converse ME coupling coefficient is given by

$$\alpha_{\mathrm{ij}}^{\mathrm{C}} = \mu_0 \frac{\partial M_{\mathrm{j}}}{\partial E_{\mathrm{i}}} \tag{3}$$

where P is polarisation, H is the applied magnetic field, μ_0 is permeability, M is magnetisation and E is the applied electric field. i is the direction of polarisation or applied electric field and j is the direction of the applied magnetic field or magnetisation. Single-phase ME materials such as antiferromagnetic chromium oxide or bismuth ferrite [5–8], were the original focus of this field, but in general they have a lower ME coefficient than ME composites, so most studies are now focussed on these materials, which couple the piezoelectric and magnetostrictive effects. Various composite forms have been fabricated such as particulate composite material systems like $BaTiO_3$-$CoFe_2O_4$ and $PbZr_x\ Ti_{(1-x)}O_3$-ferrites ($CoFe_2O_4$, NFe_2O_4) [9–12]. These were then succeeded by laminate composites because of their improved ME coefficients and lower dielectric losses such as ferrites with piezo-ceramics $PbZr_x\ Ti_{(1-x)}O_3$ [13,14], magnetic elements / alloys (Terfenol-D, Ni, Metglas) with piezo-polymers / ceramics / crystal ($PbNb_{2/3}Mg_{1/3}O_3$-$PbTiO_3$ – $PbTiO_3$, PMN-PT PZN-PT) [15,16] and magnetic elements / alloys with interdigitated

electrodes / piezo-fibres [17,18]. Carunta et al. measured α_{33}^{E} to be 284.3 mV cm^{-1} Oe^{-1} and 139.4 mV cm^{-1} Oe^{-1} for $PbTiO_3$-$NiFe_2O_4$ and $PbTiO_3$-$BiFeO_3$ thin film composites respectively and 562.1 mV cm^{-1} Oe^{-1} for an epitaxial $BaTiO_3$-$CoFe_2O_4$ film [19]. Karpinsky et al. measured α_{33}^{E} to be 0.1 mV cm^{-1} Oe^{-1} for a $BiFeO_3$-$BaTiO_3$ particulate (3-3) composite film in a 50:50 ratio [20], all from piezo-response force microscopy (PFM) measurements.[21,22]

ME composite devices convert magnetic energy to electrical energy through a two–step process: magnetic energy is first converted to mechanical energy via magnetostriction in the magnetic part of the ME composite, and then the mechanical energy is converted to electrical energy via the piezoelectric component through strain-coupling. These devices have the potential to be used in magnetic energy harvesting in light of the demand for flexible, low-cost, lightweight and even biocompatible devices [23–26].

Nanostructured ME devices have generated significant interest of late due to the possibility of enhanced ME coupling at the nanoscale. However, ME properties directly measured at the nanoscale have seldom been reported due to the non-trivial interaction of various forces at play that are difficult to accurately characterize at these length scales, including electrostatic, electrical, magnetic and electromechanical forces. In this work, (1-1) coaxial polymer-based ME composite nanowires (NWs) have been studied to determine their ME coupling using a unique sequence of scanning probe microscopy (SPM) techniques, combining atomic force microscopy (AFM), Kelvin probe force microscopy (KPFM), PFM and magnetic force microscopy (MFM) measurements. These techniques have also been used to study planar (2-2) laminate and (1-3) nanocomposite films, for comparison. The coaxial NWs studied in this work consist of magnetostrictive Ni cores surrounded by piezoelectric P(VDF-TrFE) shells, and have been fabricated from a combination of template and solution-based techniques; namely template-assisted melt-wetting to form P(VDF-TrFE) nanotubes, followed by electrodeposition of Ni inside the nanotubes. While similar techniques have been

previously used to fabricate core-shell NWs from the same combination of materials [27], their ME coupling was not measured, and specifically their ME properties were not characterized at the nanoscale. Separately, non-polymeric core-shell ME NWs such as $CoFe_2O_4$-$BaTiO_3$ (CFO-BTO) have been made via sol-gel, hydrothermal synthesis and electrospinning [28] but these all require post deposition high-temperature (> 650°C) calcination steps.

ME behaviour is affected by size, structure and crystallinity of the material. The increased surface-to-volume ratio of NWs compared to bulk, offers various advantages including enhanced elastic, piezoelectric [29–32] and ME properties [33]. ME composite NWs are more sensitive to low amplitude vibrations, have reduced fragility and increased flexibility and the increased interfacial surface area in contact between the two phases increases the strain coupling and therefore the ME coupling [33]. In the coaxial structure there is an additional advantage; the thin piezoelectric shell can absorb all or most of the magnetostrictive stress rather than just the interfacial layer which typically occurs in bulk ME composites, and also there is no substrate clamping [34]. This is also true for other core-shell structures. The polymeric nature of the NWs used here also offers a further increase in flexibility and robustness compared to non-polymeric piezoelectric materials, and are suitable for facile low-temperature, low-pressure, solution-processable fabrication techniques.

The SPM characterisation studies on ME composites which exist in the literature are mainly based on PFM. An external magnetic field from a permanent magnet is used to trigger an ME response in the composites and the piezoelectric response is measured before and after this process [19,35,36]. Some of these studies are on (1-1) core-shell CFO-BFO [36] and CFO-PZT NWs [35]. Studies on the converse ME effect exist in bulk samples, where MFM is used to image magnetic domains before and after electrical poling with the conductive AFM tip on bulk (3-3) composites [34]. Bai et al. [37] measured (1-3) composites also in the same way except they added a preliminary step to reduce electrostatic interactions encountered during the measurement,

which can interfere with any magnetic of electrical signals being measured. They measured α_{33}^{C} to be 4.9 x 10^{-9} s m^{-1} on CFO-BFO (1-3) composites. Xie et al. demonstrated two-way coupling in (2-2) composites of PZT-TbDyFe [38]. There is also an example of polymer-based (0-1) CFO-PVDF NWs where PFM was used to measure a linear change in the piezo-response under an applied magnetic field [39], however the nanoscale ME coupling has not been explored in detail.

In this work, the converse ME effect in co-axial Ni-P(VDF-TrFE) nanowires has been induced and studied using a systematic sequence of SPM characterisation techniques. Importantly, KPFM has been used to measure the surface potential of the nanowires prior to both PFM and MFM measurements, which was used to bias the AFM tip to remove the effect of surface potential[40–42]. α^{C} has also been estimated from the MFM measurements, in combination with magnetisation measurements from vibrating sample magnetometry (VSM) hysteresis loops.

Results and discussion

P(VDF-TrFE) nanotubes were fabricated via melt-wetting of nanoporous anodised aluminium oxide (AAO) templates. A thin film of P(VDF-TrFE) was spin-coated onto a glass substrate, peeled off following annealing, and placed on top of one side of the template. The film was melted while on the template and made to infiltrate the pores, followed by the process being repeated with another film on the other side of the template for complete infiltration and formation of nanotubes within the template, as schematically depicted in Figure 1a. Ni was then deposited into the P(VDF-TrFE) nanotubes while they remained vertically aligned and embedded in the template via template-assisted electrodeposition (TAED).

Prior to fabricating the (1-1) coaxial Ni-P(VDF-TrFE) NWs, the constituent P(VDF-TrFE) nanotube shells and the Ni nanowire cores were first fabricated separately as

shown in scanning electron microscope (SEM) images in Figure 1c. The main image shows the P(VDF-TrFE) shells freed from the template, while the inset shows Ni nanowire cores in cross-section still embedded within the template. Figure 1d & e are SEM images of the complete coaxial nanowires, where the P(VDF-TrFE) shell structure is more clearly visible. The metallic Ni cores are relatively bright compared to the dim polymer shells, and the figure clearly shows successful growth of the coaxial nanowires through our combination of template-assisted methods. Other template based wetting methods were attempted alongside the melt-wetting method used here to fabricate the P(VDF-TrFE) shells, including vacuum wetting. An explanation of this process as well as the fabrication details are included in the Supporting Information S1, however the melt-wetted nanotubes were found to be most robust and suitable for the subsequent infiltration of Ni by electrodeposition.

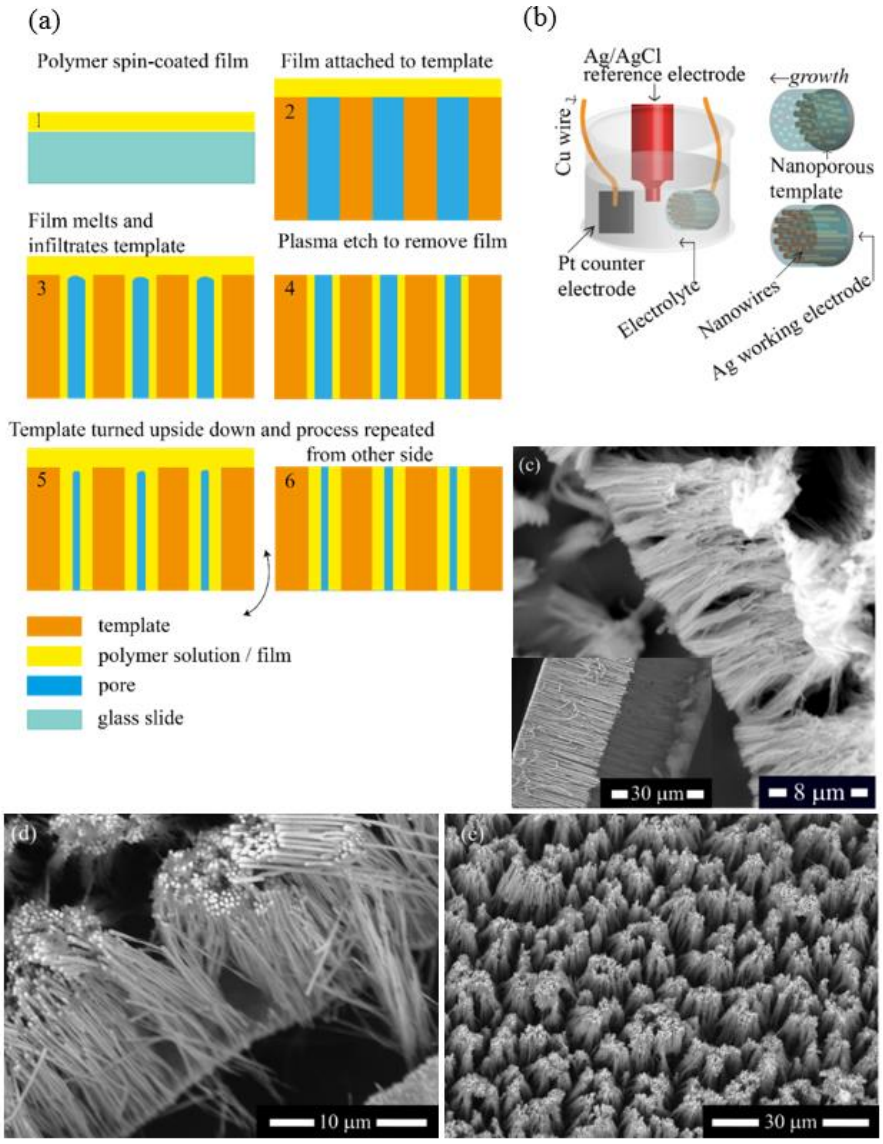

Figure 1: Schematic diagrams showing (a) the melt-wetting method used to grow P(VDF-TrFE) nanotubes and (b) template-assisted electrodeposition used to grown Ni nanowires. SEM images of (c) free P(VDF-TrFE) nanotubes with an inset of electrodeposited Ni nanowires embedded in anodic aluminium oxide templates and (d) and (e) Ni–P(VDF–TrFE) nanowires grown via melt–wetting in combination with template–assisted electrodeposition in anodic aluminium oxide templates.

The P(VDF-TrFE) nanotubes were required to predominantly form in the ferroelectric β phase, and to be polarised along the axis of the nanowires, in order for them to be useful for ME composites. Previous work in the group, including detailed structural analysis, has shown that using the nanoconfined geometry of the templates allows for the realisation of "self–poled"

highly crystalline P(VDF-TrFE) nanowires, as confinement within the template pores result in stacked ordered lamellae along the long axis of the NWs [14,43–46].

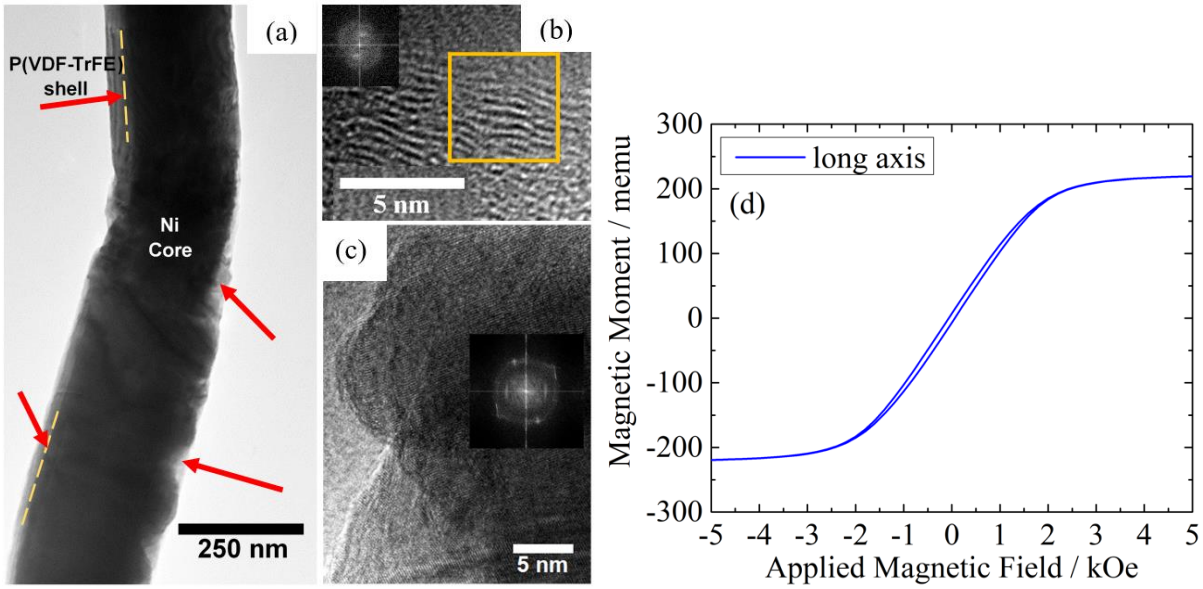

Figure 2: HR-TEM images of Ni-P(VDF-TrFE) NWs made via melt wetting and TAED: (a) complete NW; (b) shell and corresponding FFT; (c) core and corresponding FFT; (d) Vibrating sample magnetometry magnetic hysteresis curves of Ni-P(VDF-TrFE) (1-1) core-shell nanowires in an AAO template.

High resolution transmission electron microscopy (HRTEM) image of a Ni-P(VDF-TrFE) (1-1) core-shell nanowire is shown in Figure 2a. A clear boundary line can be seen near the nanowire's edge. However, the shell thickness varies along the length (shown by the dotted lines) due to the polycrystallization of Ni nanocrystals within the shell, thereby imparting a contour of varying thickness of the shell material (as shown by the arrows). The layer thicknesses are about 20 nm - 40 nm as compared to the cores, which have diameters of ≈ 190 nm - 210 nm. This variation in thicknesses in the shell was also noticed across different samples, possibly due to the differences in the filling proportion as well as the differences in the sizes and shapes of the Ni polycrystals. These showed preferred orientation of the long axis along the length of the NWs and with single crystal cubic crystallites of ~ 5 nm confirmed by HR-TEM measurements. The layer fringe pattern of the polymer shell is observed from Figure 2b, when captured from one such edge, which shows a well-defined crystalline fast Fourier

transformed (FFT) pattern (indicted in the inset of Figure 2b). This implies that the Ni nanocrystals filling inside the P(VDF-TrFE) shell might have contributed to a better P(VDF-TrFE) crystallization. Lattice fringes from the Ni nanocrystals embedded within the core-shell nanowires were also observed at lower TEM operating voltage without destroying the polymer shell (details in the methods section), as shown in Figure 2c. The inset of Figure 2c shows the FFT pattern of cubic Ni nanocrystals in the core, masked by the surrounding P(VDF-TrFE) shell pattern. These fringes are less prominent as compared to the ones observed from bare Ni polycrystalline nanowires (Supporting Information Figure S2 shows HR-TEM for both P(VDF-TrFE) shells and Ni nanowire cores individually, for comparison), which could be due to the reduced sensitivity of the polymer crystallinity to the electron radiation.

Vibrating sample magnetometry (VSM) was used to generate ferromagnetic hysteresis curves of magnetic moment as a function of applied magnetic field, and from Figure 2d, the room temperature ferromagnetic nature of Ni is clearly visible. This hysteretic nature varied depending on the structure of Ni in the sample and the orientation of the sample with respect to the direction of the applied magnetic field. For comparison, planar (2-2) and (1-3) Ni-P(VDF-TrFE) composites were also fabricated (details are included in Supporting Information sections S3 and S4 respectively, and the definitions of each type of composite structure is shown in Figure S3). The VSM results of these composite structures are also given in Supporting Information Figure S5. The saturation magnetic moment (m_S), m_R and coercive magnetic field (H_c) values for all three composite structures are given in Table 1. VSM measurements showed that magnetic hysteresis varied in Ni and Ni - P(VDF-TrFE) NWs, depending on its structure. In particular, shape anisotropy in Ni NWs led to greater remanence in the (1-3) composite when the applied magnetic field was parallel to the long NW axis rather than perpendicular to it. H_C in the (1-1) NWs was lower and so this nanocomposite was more easily magnetised than the (2-2) and (1-3) composites.

Following the detailed structural characterization and bulk magnetization measurements described above, nanoscale magnetoelectric characterization was carried out using a combination of SPM techniques. Figure 3 shows the steps in the measurement process, indicating the order in which the SPM characterisation was performed. First, KPFM was performed in order to measure the surface potential of the sample, followed by either contact mode PFM or MFM at a dc bias voltage equal to the surface potential [47], to either check the PFM signal or spatially resolve the magnetic domains before poling, respectively. Subsequently, the sample was electrically poled using a dc bias voltage applied between the AFM tip and the sample. After poling, KPFM was repeated to measure the new surface potential and PFM was performed at a dc bias voltage equal to the new surface potential, to ensure that the poling procedure had worked by observing the piezo-response of the poled region. MFM was then performed again to see if the magnetisation of the sample had changed after application of the electric field. This SPM sequence therefore constituted a direct spatially resolved measurement of the static converse ME effect, at the nanoscale. It should be noted that since the quantities of interest in this work are the magnetically associated frequency shifts (and magnetisations), we do not report the calibration of PFM and KPFM signals. The PFM operation here has two purposes: i) to electrically pole the ferroelectric polymer component of the ME composite; ii) to image the poling through an in-phase channel contrast. KPFM operation is used to measure the contact potential difference, V_{CPD}, for subsequent cancellation during PFM or MFM.

Topography images were taken alongside each of the SPM techniques used to ensure the same region of the sample was being scanned. A tip velocity of 3 μm s^{-1} was used for each scan and a poling voltage of -5 V. The dc bias voltages for MFM before poling, MFM after poling and PFM after poling were -500 mV, -800 mV and -800 mV respectively. A lift scan height of 40 nm was used for all KPFM and MFM measurements and the tip velocity

used whilst poling was 1 μm s^{-1}, previously shown suitable for ferroelectric poling of similar NWs [41] Contact mode PFM was conducted by monitoring the in-phase channel of the out-of-plane/vertical tip deflection in response to applied ac bias of 2 V at a frequency of 120 kHz.

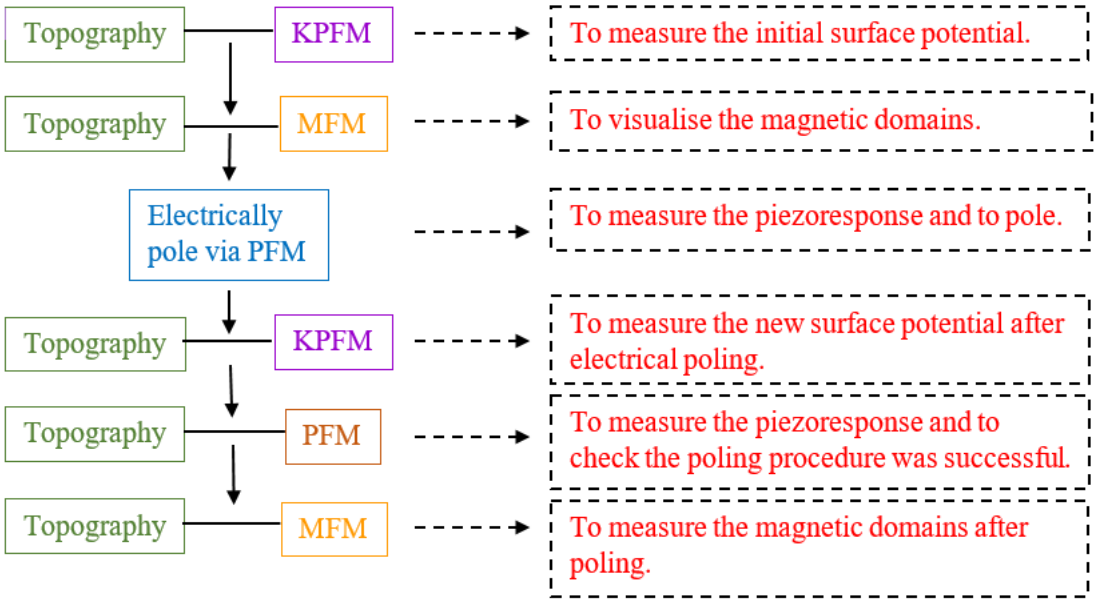

Figure 3: Process flow of SPM measurements to characterise spatially resolved nanoscale magnetoelectric properties of ME nanocomposites.

Quantitative analysis of MFM images requires the effect of the tip on the sample to be taken into account, both in terms of its shape and its magnetic properties. The method used here to approximate the ME coupling from the MFM data is based on the method used by Bai et al. [37], described as follows. Three assumptions are made: (i) the magnetic force between the tip and the sample is taken as 1D and only acting vertically in the *z*-direction, (ii) the real tip magnetisation is approximated by the point probe model [48] and (iii) the scan lift height *z* is constant so that the tip is always the same height above the sample. Under these assumptions, the magnetisation in the *z*-direction ($M_{z,i}$) is linearly related to the measured frequency shift (Δf_i) before (i = 1) and after (i = 2) poling. Notice that the dependence on tip-sample separation

is eliminated when calculating the ratio, hence the different separations still allow comparison of this quantity [35,47]. This is given by equation 4:

$$\frac{\Delta f_1}{\Delta f_2} = \frac{M_{z,1}}{M_{z,2}} \qquad (4)$$

Using the converse ME effect given by equation 3, an approximate value for α_{ij}^{C} can be calculated from equations 5 and 6:

$$\alpha_{ij}^{C} = \frac{M_{j,2}}{E_i} \qquad (5)$$

$$= \frac{\Delta f_2}{\Delta f_1}\frac{M_{j,1}}{E_i} \qquad (6)$$

This quantity has SI units of s m^{-1} [37]. E_i was taken as the poling voltage divided by the sample thickness and $M_{j,1}$ as the remanent magnetisation (M_R) from the VSM data for each sample, converted from cgs units to SI units. The value of j was determined by which M_R value used; either out-of-plane or in-plane. Δf_1 and Δf_2 were taken from the average frequency shifts of neighbouring magnetic domains from MFM images, averaged over the scan area before and after poling. This was a post-processing step. A drawback of this method is in using bulk data from the VSM in combination with the surface or nanoscale properties measured in MFM, which adds to the geometrical uncertainty of the measured values for α_{ij}^{C}. In addition, the different geometries used introduce further uncertainty in assessing the effective electric field, particularly in the case of the coaxial nanowires where the P(VDF-TrFE) shell has non-uniform thickness along the length. However, the qualitative trend in the values of α_{ij}^{C} across the different ME nanocomposites studied here remains valid.

Three line scans were used per image to find an average difference in frequency shift between peaks and troughs. Δf_1 and Δf_2 were these differences for before and after poling

respectively. The volume of the freed (1-1) nanowires on a substrate was calculated by multiplying the volume of a single nanowire by the total number of nanowires on the substrate. This number was estimated from an SEM image of the sample over a 20 μm x 20 μm square area, and then averaged and scaled up over the full substrate area.

The purpose of performing MFM was to examine the converse ME effect at the nanoscale using an SPM set-up, and therefore to see if the magnetisation changed after application of an electric field. For comparison, the results of the SPM characterisation of the (2-2) and (1-3) composites are given in the Supplementary Information section S6.

For the (1-1) core–shell nanowires, they were scanned over a small cross-section as shown in Figure 4. It is difficult to say whether this was a single nanowire or two adjacent nanowires because of the tendency of the width to be overestimated when imaging nanostructures in SPM. Even accounting for the overestimate to the width, it seems more likely that there were two nanowires because of the difference in height on the left of the images to the right side. It is possible that magnetic attraction forces bunch nanowires together. The KPFM images in Figure 4b and Figure 4f, show that the poling procedure reduced the surface potential. The contact mode in-phase channel of the PFM measurement, Figure 4h, was performed over a larger area so that the difference in the poling edges could be seen. This in-phase signal indicates the piezoelectric response in terms of amplitude and sign, relative to the applied ac bias. Calibration of the PFM signal is not required in this case, as the aim here is to apply an electric field via the AFM tip in PFM-mode. Thus the contrast along the nanowire in Fig 4h serves to indicate that poling has indeed been achieved in the area of interest. A poling V of - 5 V was used in this case, to limit damage to the the P(VDF-TrFE) shell. Higher poling voltages could be applied to the (2–2) Ni – P(VDF–TrFE) composite and the (1–3) Ni – P(VDF–TrFE) composite film, as documented in Supporting Information section S6. The MFM images before and after poling in Figure 4d and Figure 4j showed that there was a

magnetic domain, visible down the centre of the image, the magnetisation of which was altered by the poling, evident as the frequency shift increased. This is therefore direct evidence of ME coupling in this composite nanowire, where the observed change in magnetisation is due to the magnetostriction of Ni in response to the electric field-induced strain in P(VDF-TrFE) during the poling step

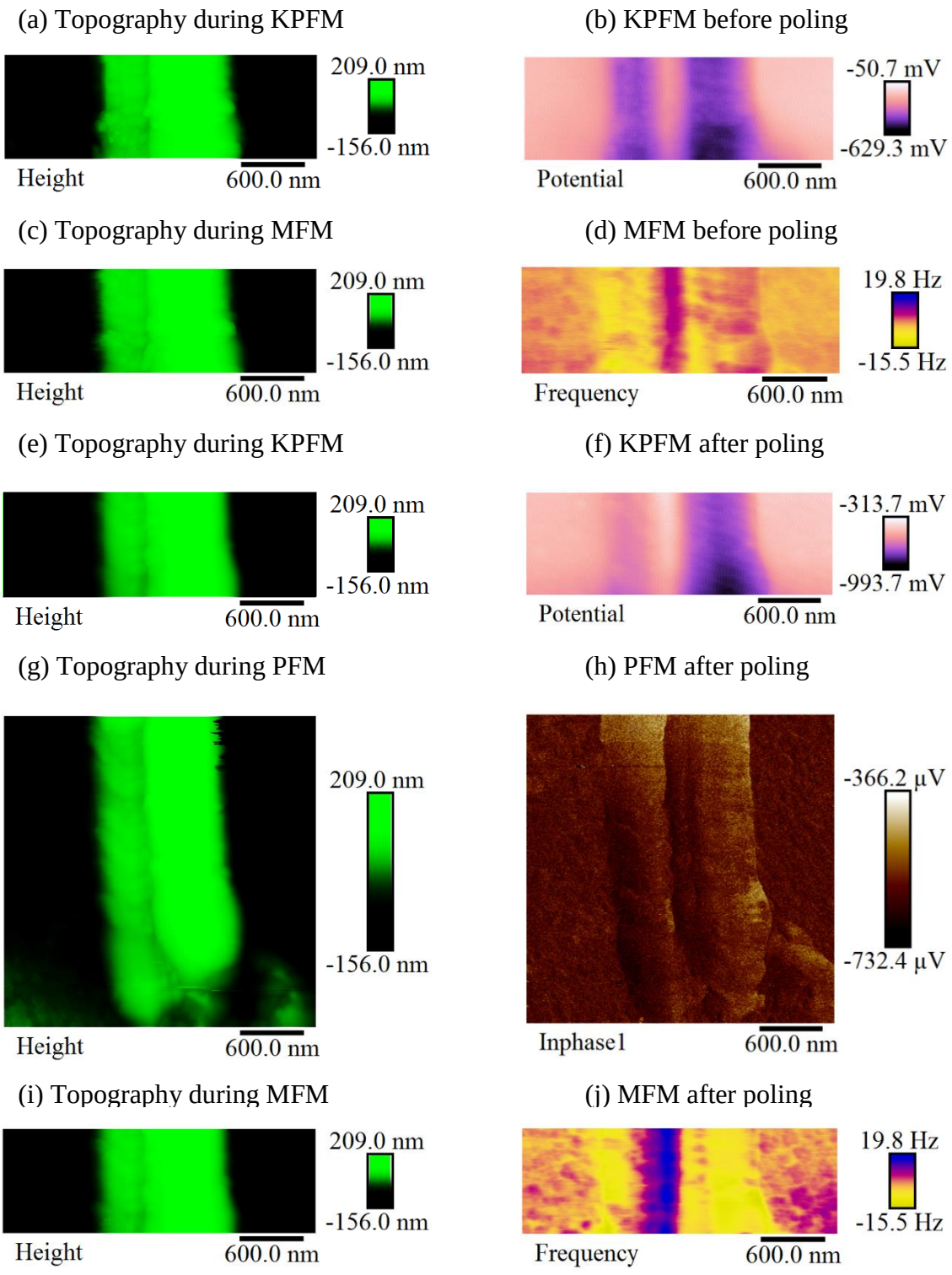

Figure 4: Scanning probe microscopy of (1-1) Ni - P(VDF-TrFE) composite nanowires scanning along the nanowire cross–section. (a), (c), (e), (g) and (i) are topography images, (b) and (h) are the corresponding Kelvin probe force microscopy images, (h) is the corresponding piezoresponse force microscopy image performed at a dc bias of - 800 mV and (d) and (j) are the corresponding magnetic force microscopy images performed at dc biases of - 500 mV and - 800 mV respectively. (a) - (d) were taken before poling at - 5 V and (e) - (j) were taken after.

Figure 5 shows a comparison of the MFM data taken before and after electrical poling across the three different composites studied. The scale bar used is the same across all images, and therefore it is clear from this figure that the greatest change in magnetization at the nanoscale, as measured directly by MFM, was observed in the coaxial Ni-P(VDF-TrFE) nanowires. Using equations 5 - 6, quantification of the ME coupling, by calculation of α^{C}, was performed using the difference in frequency shift between peaks and troughs in the MFM data both before and after poling. For the (1-1) composite, M_R was only measured parallel to the long NW axis and so this value was used for the α^{C} calculation, even though it should have been the cross-sectional value. The results are given in table 1.

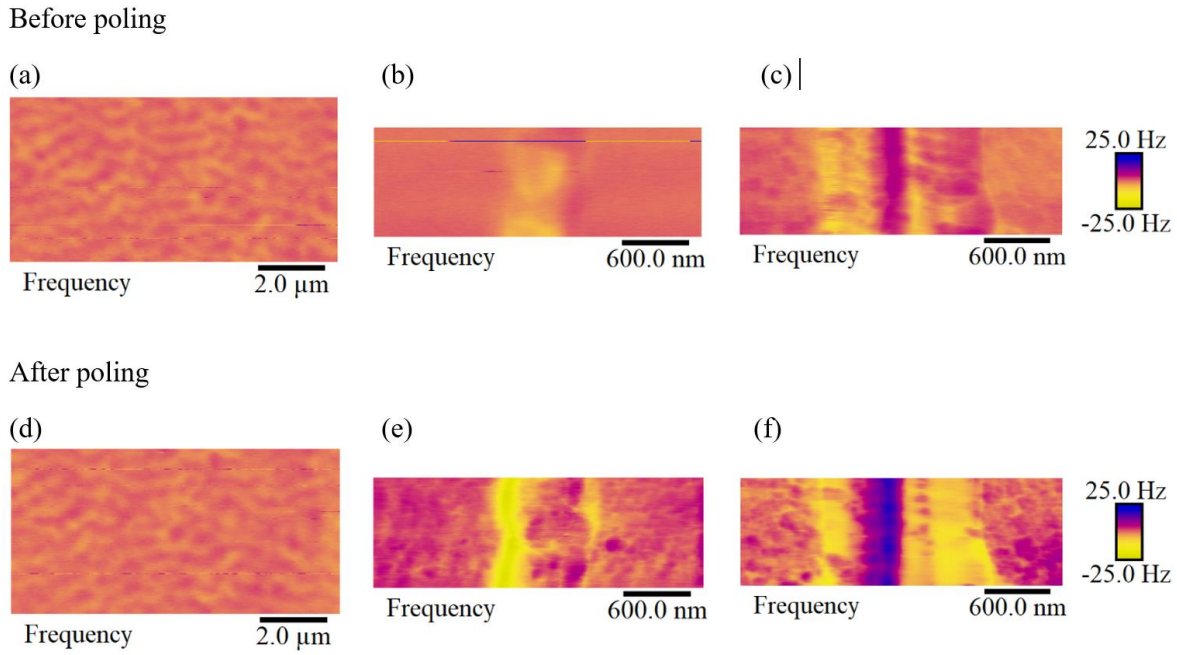

Figure 5: Magnetic force microscopy images of the (a), (d) (2-2), (b), (e) (1-3) and (c) (f) (1-1) Ni – P(VDF–TrFE) composites scanning along the NW cross-sections were relevant. The scans were performed at dc biases of (a) 360 mV, (b) 350 mV, (c) -500 mV, (d) 290 mV (e) – 500 mV and (f) -800 mV. (a) – (b) were taken before poling at - 10 V and (d) – (e) after and (e) was taken before poling at - 5V and (f) after.

In this calculation of α^{C}, the following approximations needed to be made. The m_R values used were from the VSM data, which was a bulk measurement, not a nanoscale surface measurement as in the case of the frequency shift measurements from MFM. The local surface m_R is likely to vary depending on the magnetic structure at the point of measurement compared

to the overall value for the sample. M_R was found by dividing m_R by the sample volume. There was also the uncertainty in the sample volume measurement, introduced from measuring the film thickness which was not always uniform, and thus an approximate average value was used. This was particularly true in the case of the coaxial nanowires where the P(VDF-TrFE) shell thickness was found to vary along the length. This then led to the possibility of variation in the applied electric field during poling, because even though the applied voltage was kept constant, the sample thickness, and hence field, was not uniform. It should be noted that unlike the common understanding of the ME effect as a dynamic effect, the measurements here were performed before and after ferroelectric poling – thus allowing a calculation of a static coupling coefficient. Nonetheless this should be a good measure of the dynamic behaviour as well. Finally, the MFM frequency shift was a measure of the demagnetising field from the sample, it did not take into account any other tip-sample interactions apart from the fact that electrostatic interactions had been minimised by biasing the tip with the surface potential of the sample, following KPFM.

Having stated the approximations and analysing the α^C results as they stand and considering the results presented in Table 1, it appeared that, as expected, there was ME coupling in all of the composites. All the values are quite close, in the range of a 50% deviation. The (1-1) composite NW showed the lowest coupling, followed by the (2-2) composite, and the (1-3) structure showed the largest coupling. The standard error of the mean was used to calculate the uncertainty in each α^C value. Let us now consider the geometry of the structures to analyse the results. The main differences are in the surface-to-volume ratios of the structures, and the Ni-to-polymer volume ratio, which affect the mechanical properties and surface polarisation of the different composite structures. The two extremes are the (1-3) and (1-1) composites: the former comprises a thick (140 nm) piezoelectric layer which is clamped to the surface, embedding the magnetostrictive nanowire. The latter is essentially a thin (20-40 nm)

piezoelectric shell engulfing the magnetostrictive nanowire, where the structure is mostly unclamped. The mechanical energy associated with poling a thick ferroelectric, further acting to strain the magnetostrictive material, is expected to be greater than of an unconstrained thin shell, as in the case of the coaxial nanowire. Therefore, the closeness of calculated coefficient, points out the efficient strain transfer in the (1-1) coaxial nanocomposite, suggesting high applicable potential. The 2-2 composite, where the two materials are in roughly equal geometries, forms a reference for an intermediate case, furthermore, in (2-2) laminate composites, the coupling is weakened by substrate clamping and interfacial polarisation leakage [33]. Future research directions are to directly explore the effect of core-shell thickness ratios, where the coupling can be improved. The values of i and j in α_{ij}^{C} was not clear because the direction of magnetisation at each point in the sample during MFM was unknown and they have therefore been ignored in the table and the discussion here. There are limited examples in the literature of α_{ij}^{C} measured with SPM techniques whereas there are numerous α_{ij}^{E} examples.

Table 1. Converse magnetoelectric coupling factor α^C calculated from MFM images before and after electrical poling with the AFM tip and remanent magnetisation (m_R) from VSM measurements. The sample column refers to the type of composite, the orientation defines which m_R value was used and the scan direction refers to the SPM tip scanning direction. All values are given to 2 s.f.

Sample	Orientation	m_s / memu	m_R / memu	Hc / Oe	Scan direction	Sample volume / cm^3	Electric field / Vm^{-1}	Δf_2 / Δf_1	α^C / s m^{-1}
(2–2)	out of plane	8.70	0.2	135	Across film	2.4×10^{-5}	6.7×10^7	1.4 ± 0.1	$(1.66 \pm 0.23) \times 10^{-11}$
(1–3)	cross–section	5.03×10^{-2}	1.7×10^{-2}	297	cross–section	1.1×10^{-5}	7.1×10^7	18 ± 2	$(1.87 \pm 0.25) \times 10^{-11}$
(1–1)	Long axis	221	7.1	62.6	Cross-section	1.3×10^{-3}	2.5×10^7	1.9 ± 0.1	$(1.08 \pm 0.06) \times 10^{-11}$

Conclusions

In this work, we investigated the local ME coupling in Ni - P(VDF-TrFE) coaxial NWs fabricated using a combination of template-assisted and solution-based growth techniques. The coaxial NWs fabricated via melt-wetting and TAED had varying P(VDF-TrFE) wall thickness throughout the length of the NWs but HR-TEM images confirmed that the core-shell (1-1) structure had formed. Planar (2-2) composites comprising Ni/P(VDF-TrFE) layered films, and (1-3) composites comprising Ni NWs embedded in P(VDF-TrFE) films, were also fabricated for comparison. VSM measurements indicated that the (1-1) coaxial NWs could be more easily magnetised than the (2-2) and (1-3) composites.

SPM was used to study topography, surface potential, as well as magnetisation of all three Ni - P(VDF-TrFE) ME composites, before and after a poling field was applied via the AFM tip in PFM mode. It was discovered that all three ME composites showed some degree of ME coupling, observed from the change in local magnetisation, as monitored by imaging frequency shifts during MFM, after application of an electric field which served to induce the converse ME effect. The ME coupling coefficient α^{C} was estimated for each ME composite, and they were all found to be in the same range. However, the unclamped nature of the coaxial ME nanowires, along with the lower mechanical energy associated with poling a thin ferroelectric shell suggests efficient strain transfer in the (1-1) coaxial nanocomposite structures, which can be exploited for ME applications. In particular, our fabrication method allows for scalable production of ME nanowire arrays which could be integrated into devices for ME applications, where the output can be boosted through device engineering.

In summary, we have presented a detailed study of the nanoscale magnetic properties before and after electrical poling of three geometries of Ni-P(VDF-TrFE) ME composites, namely (1-1), (1-3), (2-2). Through the application of an elaborate SPM procedure, we have managed to obtain meaningful MFM measurements, while minimising electrostatic contributions, and emphasising the effect of electrical poling. The results indicate that there is highly efficient mechanical coupling in the (1-1) coaxial nanowire structures, indicating they are favourable candidates for ME sensing and actuating applications.

Methods

Coaxial NW growth via template-assisted melt-wetting combined and electrodeposition.

P(VDF-TrFE) powder with a composition of 70:30 by weight of VDF:TrFE (Piezotech, France) was dissolved in butan-2-ol (Sigma-Aldrich) at varying concentrations between (1-10) % weight / weight (wt / wt). The solutions were placed in an ultrasonic bath for ≈ 1 hour and left overnight to ensure complete dissolution of the powder. Nanoporous anodized alumina (AAO) templates (Anodisc 25, Whatman®) were used and had nominal pore diameter, length and porosity of ≈ 200 nm, ≈ 60 μm and ≈ (25-50) % respectively. The area of the template used was ≈ 2 cm^2, which produced ~ 10^{10} NWs / NTs [43]. The 8 % wt / wt P(VDF–TrFE) solution was used for the melt-wetting synthesis of NTs. The plastic rim around the edge of the AAO templates that was used for handling was cut away with a blade and replaced with double–sided polyimide (PI) tape (3M^{TM}), as the plastic rim had a lower melting point than the temperature used during the melting process in this method. P(VDF–TrFE) films were spin-coated: 10 s at 500 revolutions per minute (rpm) followed by 1 minute at 1000 rpm (Model WS-650 Mz-23NPPB, Laurell Technologies) onto 25 mm^2 glass slides, cleaned in acetone, ethanol, IPA and DI water and dried with a compressed air gun prior to use. The films were then cured for 1 hour at 100 °C in an oven (Heratherm, ThermoFisher Scientific). The films were peeled off the glass substrates and placed on top of the templates using one film per template. The film coated templates were then placed in the oven at 185 °C for 1 hour. Plasma etching was used to remove the excess film left on top of the templates by placing the filled templates in an oxygen (25 %) / argon (75 %) plasma cleaner (Emitech K1050x) at 100 W for 40 minutes, which was found to be sufficient to remove the film without causing damage to the nanotubes. A schematic diagram of this process is shown in figure 1(a).

For electrodeposition, the electrolyte bath, there are various Ni salts which can be used as the source of Ni ions. When dissolved, they dissociate into divalent positively charged Ni^{2+} ions and when current flows, they accept two e^-s and are converted to metallic Ni on the cathode surface / working electrode [50]. At the anode, OH^- anions reduce and the main reactions at the cathode and anode are described by Eqns. 7 and 8:

$$\text{Cathode: } Ni^{2+} + 2e^- \rightarrow Ni \quad (7)$$

$$\text{Anode: } 4OH^- \rightarrow 2H_2O + O_2 + 4e^- \quad (8)$$

The most common bath to be used is the Watts bath: nickel sulphate ($NiSO_4$), nickel chloride ($NiCl_2$) and boric acid (H_3BO_3) but here a variation of this, without the $NiCl_2$ has been used to make the preparation safer. Instead, the electrolyte contained 100 ml of $NiSO_4$ (120 g/L) (98 % Alfa Aesar) and H_3BO_3 (45 g/L) (+ 99 % Alfa Aesar) in DI water with a pH 4.5, measured with pH paper (Panphea), at room temperature (22 °C). The salt was dissolved in DI water using a magnetic follower on a hotplate / magnetic stirrer and heated to 40 °C to speed up the dissolution. The H_3BO_3 in the electrolyte acted as a pH buffer; it prevented the cathode from becoming too alkaline [51] as the pH tended to increase from discharge of H^+ ions, which liberated H_2 gas. H_3BO_3 limited the effect on the pH that the gas release had [50].

For template-assisted electrodeposition (TAED) of Ni, a ~ 100 nm Ag electrode was sputter-deposited on one side of the P(VDF-TrFE) nanotube-filled AAO template at 40 mA for 4 minutes. A circular shadow mask was used to sputter a ≈ 3 cm^3 area on the ≈ 5 cm^2 template and a Cu wire was attached with Cu tape and then the whole surface was covered with PI tape. The deposition voltage used was - 1.0 V for 5025 s and after the deposition, the same melt–wetting process was repeated from the other side of the template using a second film. Finally,

the filled templates were cured for 12 hours at 100 °C to improve the crystallinity of the NTs. A schematic diagram of this process is given in figure 1(b).

Sample preparation for scanning electron microscopy (SEM) and transmission electron microscopy (TEM) and measurement details.

Two field emission floor model SEMs were used: a Leo Gemini 1530VP Variable Pressure (Zeiss) was used with an in‑lens detector and an accelerating V of 5 keV ‑ 10 keV and a Nova NanoSEM (FEI). The NWs and NTs were imaged both from top–down freed from the template and in cross–section whilst still in the template. Each sample was fixed to an SEM stub with C tape (Agar Scientific) and a < 10 nm thick layer of palladium (Pd) was sputter‑deposited using a sputter coater (K575, EMITECH) at 40 mA for 20 s. For imaging the freed P(VDF-TrFE) NTs, the samples were prepared by breaking the NT-filled templates into ≈ 1 mm^2 pieces with tweezers and the pieces of filled template were stuck directly to SiO_2 wafer prior to being submerged in 12.5 % wt / wt phosphoric acid in DI water (from 80 %, Sigma-Aldrich) for 3 hours. For imaging the Ni NWs in the template in cross-section, the pieces were stuck directly to the SiO_2 wafer. The core-shell NWs were imaged both in cross-section and top-down and freed from the template. The freeing process was the same as for the NTs.

For high resolution–TEM (HR-TEM) imaging of the freed Ni–P(VDF-TrFE) NWs, Tecnai T20 microscope equipped with a Gatan Imaging Filter was used and to release them into a solution and deposited onto pieces of SiO_2 wafer. The accelerating V used was 120 kV with a spot size of 3. To prevent substantial damage caused by the electron beam and was alternated between 100 kV and 120 kV. To release them into a solution, pieces of template were submerged in 2 mL of 40 % wt / wt phosphoric acid in DI water in centrifuge vials (Sigma–Aldrich) with a 7 mm x 2 mm magnetic follower and left on a magnetic stirrer / hotplate for 5.5 hours. The vials were topped up with DI water and placed in a centrifuge

(Sigma 1–14 Microfuge) for 1 hour 15 minutes at 14000 rpm. This resulted in the NWs collecting at the bottom of the vial and allowed for the phosphoric acid solution to be removed and replaced with DI water leaving freed NWs suspended in DI water. This acid removal / cleaning process was repeated three times followed by adding 0.5 ml of absolute ethanol (analytical reagent grade, Fisher Scientific) into the centrifuge vial. After placing this in an ultrasonic bath (U50, Ultrawave) for ≈ 3 s, a droplet was then drop–cast onto a Cu coated TEM grid and naturally dried in air for 20 minutes.

Sample preparation for VSM and measurement details.

Princeton Measurements Corporation electromagnets with an Applied Magnetics Laboratory Inc. Precision Bipolar Magnet Controller and a Princeton Measurements Corporation MicroMag Controller were the components of the VSM used. The maximum uniform H available was 10 kOe and the magnetic moment sensitivity range was 10 μemu – 2 emu. The core-shell NW –filled template was attached to a sample holder at the end of a cylindrical probe with PI tape and the probe was clamped between the centre of the pickup coils so that the direction of the magnetic field was aligned parallel to the long NW axis of the NW arrays. The probe was vibrated at 83 Hz with an amplitude of 1.0 mm and a continuous magnetic field sweep was used with a pause of 300 ms after each step increment. The maximum applied magnetic field was 10 kOe, the field increment of the sweep was 200 Oe, the sensitivity / range of the magnetic moment measured by the Hall probe was 500 memu and the averaging time of each measurement was 1s.

Sample preparation for SPM and measurement details.

A Multimode VIII with a Nanoscope V controller and Nanoscope 8.15 software (Bruker) was used and all experiments were performed with the same tips: MESP-RC-V2 (Bruker) with nominal spring constant 5 Nm^{-1}, a resonance frequency of ~ 150 kHz and a Co / chromium

(Cr) ferromagnetic coating. The NWs were released from the template as described above except isopropyl alcohol (Fisher chemical) was used to disperse them and they were drop-cast onto ITO coated glass (Sigma-Aldrich) substrates of 15 mm x 15 mm x 1.1 mm. The substrate was then mounted onto a 12 mm diameter metallic disc designed for loading into the AFM and Ag conductive paint was used to electrically connect an exposed area of the ITO on the substrate to the disc which then acted as the bottom / sample electrode in KPFM and PFM measurements.

Associated Content

Supporting Information available: S1 - vacuum-wetting fabrication method to prepare P(VDF-TrFE) nanotubes, S2 – Template assisted electrodeposition of Ni nanowires , S3 - (2-2) Ni - (PVDF-TrFE) laminate fabrication method, S4 - (1-3) Ni – P(VDF-TrFE) nanocomposite fabrication method, S5 - HR-TEM images of P(VDF-TrFE) NTs and Ni nanowies and S6 – Variable Sample Magnetometry and Scanning Probe Microscopy results of (2-2) and (1-3) Ni-P(VDF-TrFE) composites.

Acknowledgements

S.K-N acknowledges financial support from the European Research Council through an ERC Starting Grant (Grant No. ERC-2014-STG-639526, NANOGEN). C.B acknowledges funding from the EPSRC Cambridge NanoDTC, EP/G037221/1, Cambridge Philosophical Society bursary, Sir Colin Corness Bursary from Magdalene College Cambridge and EPSRC post-PhD prize. A.D. also acknowledges financial support from The Department of Science and Technology (DST) - Science & Engineering Research Board (SERB), India “Ramanujan Fellowship” (Award No. SB/S2/RJN-057/2017).

References

(1) Roundy, S.; Leland, E. S.; Baker, J.; Carleton, E.; Reilly, E.; Lai, E.; Otis, B.; Rabaey, J. M.; Wright, P. K.; Sundararajan, V. Improving Power Output for Vibration-Based Energy Scavengers. *IEEE Pervasive Comput.* **2005**, *4* (1), 28–36. https://doi.org/10.1109/MPRV.2005.14.

(2) Cook-Chennault, K. A.; Thambi, N.; Sastry, A. M. Powering MEMS Portable Devices - a Review of Non-Regenerative and Regenerative Power Supply Systems with Special Emphasis on Piezoelectric Energy Harvesting Systems. *Smart Mater. Struct.* **2008**, *17* (4), 043001. https://doi.org/10.1088/0964-1726/17/4/043001.

(3) Horton, W. F.; Goldberg, S. *Power Frequency Magnetic Fields and Public Health*; CRC Press, 1995.

(4) Boughey, C.; Kar-Narayan, S. Energy Harvesting. In *Magnetoelectric Polymer-Based Composites: Fundamentals and Applications*; Lanceros-Méndez, S., Martins, P., Eds.; Wiley-VCH Verlag GmbH & Co. KGaA, 2017; pp 197–224. https://doi.org/10.1002/9783527801336.ch6c.

(5) Dzyaloshinskii, I. E. On the Magneto-Electrical Effect in Antiferromagnets. *Sov. Phys. J. Exp. Theor. Phys.* **1960**, *10* (3), 628–629.

(6) Astrov, D. N. The Magnetoelectric Effect in Antiferromagnetics. *Sov. Phys. J. Exp. Theor. Phys.* **1960**, *11* (3), 708–709.

(7) Vaz, C. A. F.; Hoffman, J.; Ahn, C. H.; Ramesh, R. Magnetoelectric Coupling Effects in Multiferroic Complex Oxide Composite Structures. *Adv. Mater.* **2010**, *22* (26–27), 2900–2918. https://doi.org/10.1002/adma.200904326.

(8) Kadomtseva, A. M.; Krotov, S. S.; Popov, Y. F.; Vorob'ev, G. P. Features of the Magnetoelectric Behavior of the Family of Multiferroics RMn2O5 at High Magnetic Fields (Review). *Low Temp. Phys.* **2006**, *32* (8), 709–724. https://doi.org/10.1063/1.2219494.

(9) Run, A. M. J. G. V.; Terrell, D. R.; Scholing, J. H. An in Situ Grown Eutectic Magnetoelectric Composite Material. *J. Mater. Sci.* **1974**, *9* (10), 1710–1714. https://doi.org/10.1007/BF00540771.

(10) Srinivasan, G.; Rasmussen, E. T.; Gallegos, J.; Srinivasan, R.; Bokhan, Y. I.; Laletin, V. M. Magnetoelectric Bilayer and Multilayer Structures of Magnetostrictive and Piezoelectric Oxides. *Phys. Rev. B* **2001**, *64* (21), 214408. https://doi.org/10.1103/PhysRevB.64.214408.

(11) Nan, C.-W. Magnetoelectric Effect in Composites of Piezoelectric and Piezomagnetic Phases. *Phys. Rev. B* **1994**, *50* (9), 6082–6088. https://doi.org/10.1103/PhysRevB.50.6082.

(12) Benveniste, Y. Magnetoelectric Effect in Fibrous Composites with Piezoelectric and Piezomagnetic Phases. *Phys. Rev. B* **1995**, *51* (22), 16424–16427. https://doi.org/10.1103/PhysRevB.51.16424.

(13) Lee, S.; Lee, B.; Choi, J.; Chi, C.-S.; Jeong, Y.; Oh, H.-J. Effects of Various Solution Wetting Conditions on the Morphology and the Crystallization of Poly(Vinylidene Fluoride) Nanotubes. *J. Korean Phys. Soc.* **2009**, *54* (3), 1198–1202.

(14) Cauda, V.; Dapra, D.; Aulika, I.; Chiodoni, A.; Demarchi, D.; Civera, P.; Pizzi, M. Distributed Array of Polymeric Piezo-Nanowires through Hard-Templating Method into Porous Alumina. *Sens. Transducers* **2011**, *12* (Special), 11–7.

(15) Dong, S.; Zhai, J.; Xing, Z.; Li, J.; Viehland, D. Giant Magnetoelectric Effect (under a Dc Magnetic Bias of 2 Oe) in Laminate Composites of FeBSiC Alloy Ribbons and $Pb(Zn_{1/3},Nb_{2/3})O_3$ – 7 % $PbTiO_3$ Fibers. *Appl. Phys. Lett.* **2007**, *91* (2), 022915. https://doi.org/10.1063/1.2757146.

(16) Wang, Y.; Hasanyan, D.; Li, J.; Viehland, D.; Luo, H. Shear-Mode Magnetostrictive/Piezoelectric Composite with an Enhanced Magnetoelectric Coefficient. *Appl. Phys. Lett.* **2012**, *100* (20), 202903. https://doi.org/10.1063/1.4718352.

(17) Li, M.; Wang, Y.; Gao, J.; Gray, D.; Li, J.; Viehland, D. Dependence of Magnetic Field Sensitivity of a Magnetoelectric Laminate Sensor Pair on Separation Distance: Effect of Mutual Inductance. *J. Appl. Phys.* **2012**, *111* (3), 033923. https://doi.org/10.1063/1.3684986.

(18) Hasanyan, D.; Gao, J.; Wang, Y.; Viswan, R.; Li, M.; Shen, Y.; Li, J.; Viehland, D. Theoretical and Experimental Investigation of Magnetoelectric Effect for Bending-Tension Coupled Modes in Magnetostrictive-Piezoelectric Layered Composites. *J. Appl. Phys.* **2012**, *112* (1), 013908. https://doi.org/10.1063/1.4732130.
(19) Caruntu, G.; Yourdkhani, A.; Vopsaroiu, M.; Srinivasan, G. Probing the Local Strain-Mediated Magnetoelectric Coupling in Multiferroic Nanocomposites by Magnetic Field-Assisted Piezoresponse Force Microscopy. *Nanoscale* **2012**, *4* (10), 3218–3227. https://doi.org/10.1039/C2NR00064D.
(20) Karpinsky, D. V.; Pullar, R. C.; Fetisov, Y. K.; Kamentsev, K. E.; Kholkin, A. L. Local Probing of Magnetoelectric Coupling in Multiferroic Composites of $BaFe_{12}O_{19}$ – $BaTiO_3$. *J. Appl. Phys.* **2010**, *108* (4), 042012. https://doi.org/10.1063/1.3474967.
(21) Pan, M.; Liu, Y.; Bai, G.; Hong, S.; Dravid, V. P.; Petford-Long, A. K. Structure-Property Relationships in Self-Assembled Metalorganic Chemical Vapor Deposition–Grown CoFe2O4–PbTiO3 Multiferroic Nanocomposites Using Three-Dimensional Characterization. *J. Appl. Phys.* **2011**, *110* (3), 034103. https://doi.org/10.1063/1.3615888.
(22) Pan, M.; Hong, S.; Guest, J. R.; Liu, Y.; Petford-Long, A. Visualization of Magnetic Domain Structure Changes Induced by Interfacial Strain in CoFe 2 O 4 /BaTiO 3 Heterostructures. *J. Phys. Appl. Phys.* **2013**, *46* (5), 055001. https://doi.org/10.1088/0022-3727/46/5/055001.
(23) Reis, S.; Silva, M. P.; Castro, N.; Correia, V.; Rocha, J. G.; Martins, P.; Lasheras, A.; Gutierrez, J.; Lanceros-Mendez, S. Electronic Optimization for an Energy Harvesting System Based on Magnetoelectric Metglas/Poly(Vinylidene Fluoride)/Metglas Composites. *Smart Mater. Struct.* **2016**, *25* (8), 085028. https://doi.org/10.1088/0964-1726/25/8/085028.
(24) Qi, Y.; Jafferis, N. T.; Lyons, K.; Lee, C. M.; Ahmad, H.; McAlpine, M. C. Piezoelectric Ribbons Printed onto Rubber for Flexible Energy Conversion. *Nano Lett.* **2010**, *10* (2), 524–528. https://doi.org/10.1021/nl903377u.
(25) Martins, P.; Lanceros-Méndez, S. Polymer-Based Magnetoelectric Materials. *Adv. Funct. Mater.* **2013**, *23* (27), 3371–3385. https://doi.org/10.1002/adfm.201202780.
(26) Sue, C.-Y.; Tsai, N.-C. Human Powered MEMS-Based Energy Harvest Devices. *Appl. Energy* **2012**, *93*, 390–403. https://doi.org/10.1016/j.apenergy.2011.12.037.
(27) Sun, C.-L.; Lam, K. H.; Chao, C.; Lau, S. T.; Chan, H. L. W.; Guo, S.; Zhao, X. Fabrication and Characterization of Ni*/*P(VDF-TrFE) Nanoscaled Coaxial Cables. *Appl. Phys. Lett.* **2007**, *90* (25), 253107. https://doi.org/10.1063/1.2750391.
(28) Raidongia, K.; Nag, A.; Sundaresan, A.; Rao, C. N. R. Multiferroic and Magnetoelectric Properties of Core-Shell CoFe2O4@BaTiO3 Nanocomposites. *Appl. Phys. Lett.* **2010**, *97* (6), 062904. https://doi.org/10.1063/1.3478231.
(29) Boxberg, F.; Søndergaard, N.; Xu, H. Q. Elastic and Piezoelectric Properties of Zincblende and Wurtzite Crystalline Nanowire Heterostructures. *Adv. Mater. Deerfield Beach Fla* **2012**, *24* (34), 4692–4706. https://doi.org/10.1002/adma.201200370.
(30) Kalinin, S. V.; Bonnell, D. A.; Alvarez, T.; Lei, X.; Hu, Z.; Ferris, J. H.; Zhang, Q.; Dunn, S. Atomic Polarization and Local Reactivity on Ferroelectric Surfaces : A New Route toward Complex Nanostructures. *Nano Lett.* **2002**, *2* (6), 589–93. https://doi.org/10.1021/nl025556u.
(31) Williamson, B. J.; Pastiroff, S.; Cressey, G. Piezoelectric Properties of Quartz and Cristobalite Airborne Particulates as a Cause of Adverse Health Effects. *Atmos. Environ.* **2001**, *35* (20), 3539–42. https://doi.org/10.1016/S1352-2310(01)00121-2.
(32) Espinosa, H. D.; Bernal, R. A.; Minary-Jolandan, M. A Review of Mechanical and Electromechanical Properties of Piezoelectric Nanowires. *Adv. Mater.* **2012**, *24* (34), 4656–75. https://doi.org/10.1002/adma.201104810.
(33) Andrew, J. S.; Starr, J. D.; Budi, M. A. K. Prospects for Nanostructured Multiferroic Composite Materials. *Scr. Mater.* **2014**, *74*, 38–43. https://doi.org/10.1016/j.scriptamat.2013.09.023.
(34) Zheng, T.; Zong, Y.; Yue, Z.; Wallace, G. G.; Higgins, M. J. Magnetoelectric Composites for Bionics Applications. In *Magnetoelectric Polymer-Based Composites*; Lanceros-Méndez, S., Pedrortins, Eds.; Wiley-VCH Verlag GmbH & Co. KGaA, 2017; pp 171–195. https://doi.org/10.1002/9783527801336.ch6b.

(35) Xie, S.; Ma, F.; Liu, Y.; Li, J. Multiferroic $CoFe_2O_4$ – $Pb(Zr_{0.52}Ti_{0.48})O_3$ Core-Shell Nanofibers and Their Magnetoelectric Coupling. *Nanoscale* **2011**, *3* (8), 3152–3158. https://doi.org/10.1039/C1NR10288E.
(36) Zhu, Q.; Xie, Y.; Zhang, J.; Liu, Y.; Zhan, Q.; Miao, H.; Xie, S. Multiferroic $CoFe_2O_4$ – $BiFeO_3$ Core–Shell Nanofibers and Their Nanoscale Magnetoelectric Coupling. *J. Mater. Res.* **2014**, *29* (5), 657–664. https://doi.org/10.1557/jmr.2014.36.
(37) Bai, F.; Zhang, H.; Li, J.; Viehland, D. Magnetic and Magnetoelectric Properties of As-Deposited and Annealed $BaTiO_3$ – $CoFe_2O_4$ Nanocomposite Thin Films. *J. Phys. Appl. Phys.* **2010**, *43* (28), 285002. https://doi.org/10.1088/0022-3727/43/28/285002.
(38) Xie, S. H.; Liu, Y. M.; Liu, X. Y.; Zhou, Q. F.; Shung, K. K.; Zhou, Y. C.; Li, J. Y. Local Two-Way Magnetoelectric Couplings in Multiferroic Composites via Scanning Probe Microscopy. *J. Appl. Phys.* **2010**, *108* (5), 054108. https://doi.org/10.1063/1.3481459.
(39) Gonçalves, R.; Martins, P.; Moya, X.; Ghidini, M.; Sencadas, V.; Botelho, G.; Mathur, N. D.; Lanceros-Mendez, S. Magnetoelectric $CoFe_2O_4$ / Polyvinylidene Fluoride Electrospun Nanofibres. *Nanoscale* **2015**, *7* (17), 8058–8061. https://doi.org/10.1039/C5NR00453E.
(40) Jaafar, M.; Iglesias-Freire, O.; Serrano-Ramón, L.; Ibarra, M. R.; de Teresa, J. M.; Asenjo, A. Distinguishing Magnetic and Electrostatic Interactions by a Kelvin Probe Force Microscopy–Magnetic Force Microscopy Combination. *Beilstein J. Nanotechnol.* **2011**, *2*, 552–560. https://doi.org/10.3762/bjnano.2.59.
(41) Arenas, M. P.; Lanzoni, E. M.; Pacheco, C. J.; Costa, C. A. R.; Eckstein, C. B.; de Almeida, L. H.; Rebello, J. M. A.; Deneke, C. F.; Pereira, G. R. Separating the Influence of Electric Charges in Magnetic Force Microscopy Images of Inhomogeneous Metal Samples. *J. Magn. Magn. Mater.* **2018**, *446*, 239–244. https://doi.org/10.1016/j.jmmm.2017.09.041.
(42) Milde, P.; Neuber, E.; Bauer, A.; Pfleiderer, C.; Berger, H.; Eng, L. M. Heuristic Description of Magnetoelectricity of Cu2OSeO3. *Nano Lett.* **2016**, *16* (9), 5612–5618. https://doi.org/10.1021/acs.nanolett.6b02167.
(43) Whiter, R. A.; Narayan, V.; Kar-Narayan, S. A Scalable Nanogenerator Based on Self-Poled Piezoelectric Polymer Nanowires with High Energy Conversion Efficiency. *Adv. Energy Mater.* **2014**, *4* (18), 1400519. https://doi.org/10.1002/aenm.201400519.
(44) Whiter, R. A.; Calahorra, Y.; Ou, C.; Kar-Narayan, S. Observation of Confinement-Induced Self-Poling Effects in Ferroelectric Polymer Nanowires Grown by Template Wetting. *Macromol. Mater. Eng.* **2016**, *301* (9), 1016–1025. https://doi.org/10.1002/mame.201600135.
(45) Whiter, R. A.; Boughey, C.; Smith, M.; Kar-Narayan, S. Mechanical Energy Harvesting Performance of Ferroelectric Polymer Nanowires Grown via Template-Wetting. *Energy Technol.* **2018**. https://doi.org/10.1002/ente.201700820.
(46) Calahorra, Y.; Whiter, R. A.; Jing, Q.; Narayan, V.; Kar-Narayan, S. Localized Electromechanical Interactions in Ferroelectric P(VDF-TrFE) Nanowires Investigated by Scanning Probe Microscopy. *APL Mater.* **2016**, *4* (11), 116106. https://doi.org/10.1063/1.4967752.
(47) Kim, S.; Seol, D.; Lu, X.; Alexe, M.; Kim, Y. Electrostatic-Free Piezoresponse Force Microscopy. *Sci. Rep.* **2017**, *7*, 41657. https://doi.org/10.1038/srep41657.
(48) Wright, C. D.; Hill, E. W. Reciprocity in Magnetic Force Microscopy. *Appl. Phys. Lett.* **1995**, *67* (3), 433–435. https://doi.org/10.1063/1.114623.
(49) Häberle, T.; Haering, F.; Pfeifer, H.; Han, L.; Kuerbanjiang, B.; Wiedwald, U.; Ulrich Herr; Koslowski, B. Towards Quantitative Magnetic Force Microscopy: Theory and Experiment. *New J. Phys.* **2012**, *14* (4), 043044. https://doi.org/10.1088/1367-2630/14/4/043044.
(50) Rose, I.; Whittington, C. Nickel Plating Handbook https://www.nickelinstitute.org/~/media/Files/TechnicalLiterature/NPH_141015.ashx.
(51) Yin, K.-M.; Lin, B.-T. Effects of Boric Acid on the Electrodeposition of Iron, Nickel and Iron-Nickel. *Surf. Coat. Technol.* **1996**, *78* (1), 205–210. https://doi.org/10.1016/0257-8972(94)02410-3.

TOC

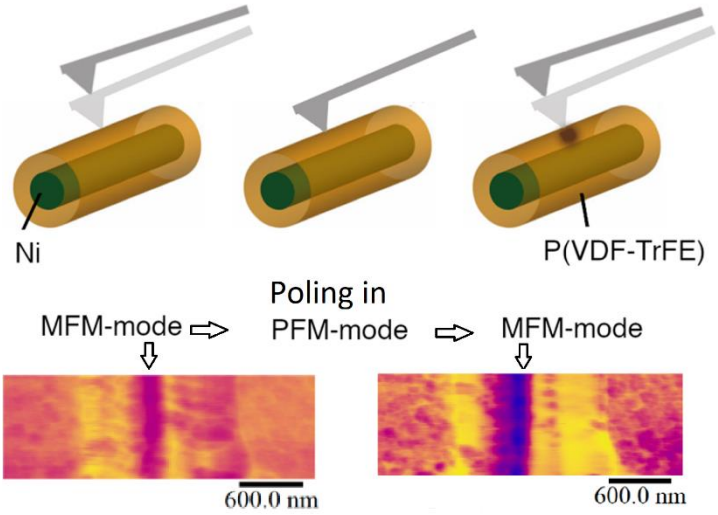
Ni
P(VDF-TrFE)
Poling in
PFM-mode
MFM-mode
MFM-mode
600.0 nm
600.0 nm